JACS
JOURNAL OF THE AMERICAN CHEMICAL SOCIETY
pubs.acs.org/JACS
Article

Predicting Mutational Effects on Ca^{2+}-Activated Chloride Conduction of TMEM16A Based on a Simulation Study

Yue Zhang, Kang Wu, Yuqing Li, Song Wu,* Arieh Warshel,* and Chen Bai*

Cite This: J. Am. Chem. Soc. 2024, 146, 4665−4679
Read Online

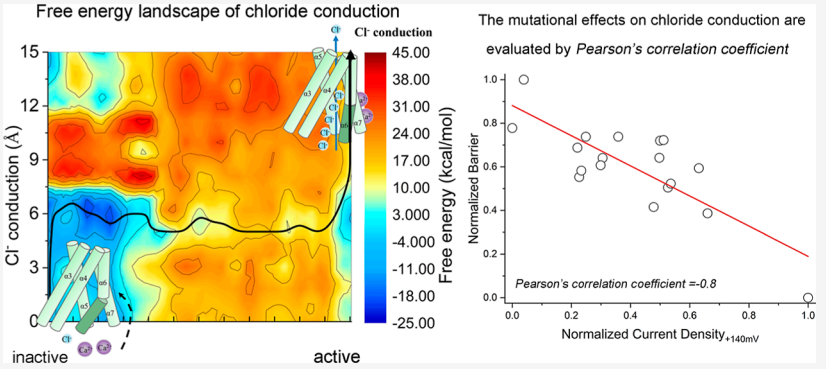

ABSTRACT: The dysfunction and defects of ion channels are associated with many human diseases, especially for loss-of-function mutations in ion channels such as cystic fibrosis transmembrane conductance regulator mutations in cystic fibrosis. Understanding ion channels is of great current importance for both medical and fundamental purposes. Such an understanding should include the ability to predict mutational effects and describe functional and mechanistic effects. In this work, we introduce an approach to predict mutational effects based on kinetic information (including reaction barriers and transition state locations) obtained by studying the working mechanism of target proteins. Specifically, we take the Ca^{2+}-activated chloride channel TMEM16A as an example and utilize the computational biology model to predict the mutational effects of key residues. Encouragingly, we verified our predictions through electrophysiological experiments, demonstrating a 94% prediction accuracy regarding mutational directions. The mutational strength assessed by Pearson's correlation coefficient is −0.80 between our calculations and the experimental results. These findings suggest that the proposed methodology is reliable and can provide valuable guidance for revealing functional mechanisms and identifying key residues of the TMEM16A channel. The proposed approach can be extended to a broad scope of biophysical systems.

1. INTRODUCTION

Proteins are vital biomacromolecules that function in most biological processes. The proper functioning of proteins is significant for human health. Mutations can influence protein folding,[1] stability,[2] expression,[3] function,[4] interactions with other biomolecules,[5] subcellular localization,[6] and even lead to severe diseases, such as cancers[7] or neurodegenerative diseases,[8] etc. Investigating mutational effects could help reveal the protein's functional mechanism, understand the biological process, and shed light on disease treatments and drug development. Therefore, identifying mutational effects quickly and accurately has vital scientific significance.

Experimental studies can determine mutational effects, but they are usually expensive and time-consuming. Thus, it is of broad interest to predict mutational effects in a short time with sufficient accuracy. Over the years, multiple methods have been developed for predictions and understanding of mutational effects by analyzing physicochemical properties, e.g., charge, polarity, and hydrophobicity, as well as structural features, e.g., the side chain length and aromaticity of amino acids.[9] These methods can be divided into machine learning (ML)[10] and molecular simulations (MS) algorithms.[11,12] ML algorithms integrate properties of the original and mutant residues, such as charge, polarity, and hydrophobicity, structural information, and evolutionary conservation. The ML model is then trained on the available data to distinguish the functional mutations (that have obvious effects on biological function) and neutral mutations (that have little influence on biological function).[13] ML is less dependent on the 3D protein structures than MS algorithms.[14] However,

Received: October 26, 2023
Revised: January 10, 2024
Accepted: January 11, 2024
Published: February 6, 2024

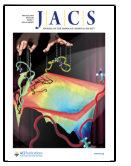

https://doi.org/10.1021/jacs.3c11940
J. Am. Chem. Soc. 2024, 146, 4665−4679

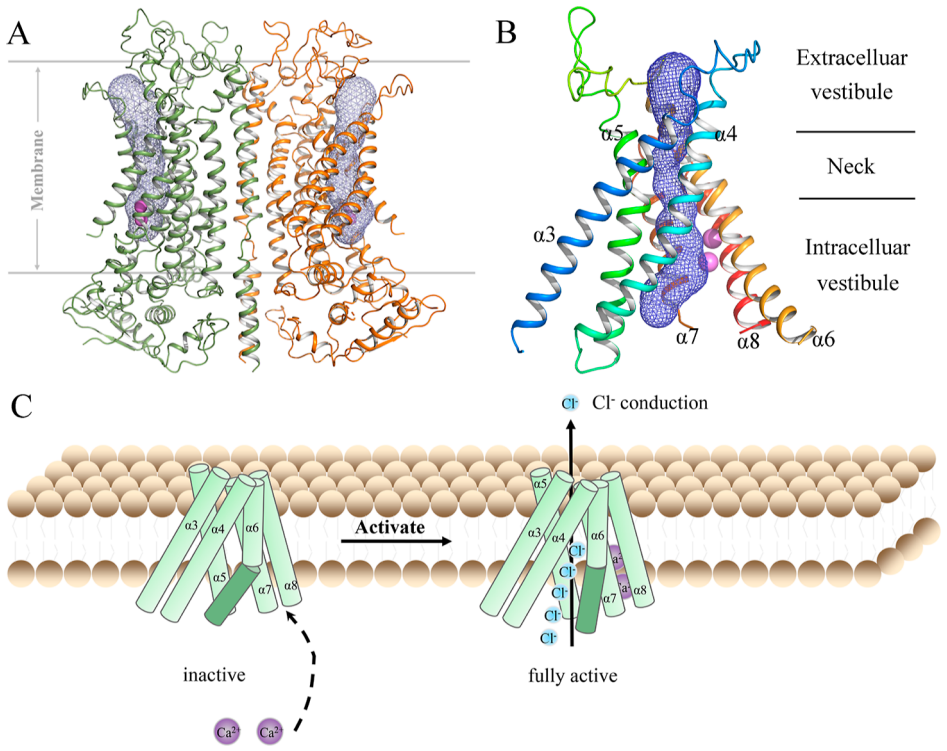

Figure 1. TMEM16A structures and Ca^{2+}-activated chloride conduction pathway. (A) Dimer structure of the TMEM16A channel (PDB ID:7B5C, fully active state). Two subunits of the dimer are colored green and orange, while pink spheres show Ca^{2+} ions. The blue mesh represents the Cl^- ion entry path through the vestibule region. (B) Ion conduction pore of the TMEM16A channel (fully active state). (C) Schematic representation of the Ca^{2+}-activated chloride conduction across the membrane. The binding of two Ca^{2+} ions induces the movement of the inner half of the $\alpha 6$ helix. The movement propagates to the neck region and opens the channel pore to allow the transduction of chloride ions.

some performance evaluation of ML algorithms failed to reproduce high accuracies,[14,15] and none of the predicted mutations is experimentally verified in a blind prospective validation.[16] Unlike ML algorithms, MS algorithms rely on 3D protein structures and perform better in experimental validations.[17] However, MS algorithms also have limitations since the simulation protein functions require specialized approaches and involve convergence problems. For example, in processes that involve large conformational changes, it is important to evaluate the corresponding activation path and the relevant activation barrier. Thus, it is challenging to accurately model the activation processes of large biophysical systems and predict their mutational effects.

A challenging system is the family of ion channels, which is relevant to regulating transmembrane electrical potentials and important in multiple physiological functions.[18−21] The dysfunctional ion channels can cause diseases in many tissues. For example, mutations in the Piezo1 ion channel are related to dehydrated hereditary xerocytosis, congenital lymphatic dysplasia, and pancreatitis.[22] R117H in the cystic fibrosis transmembrane conductance regulator chloride channel is common in cystic fibrosis patients worldwide.[23] Investigating mutational effects considerably fosters our understanding of physiological and pathophysiological processes. An excellent example in this family is the prominent Ca^{2+}-activated chloride channel, TMEM16A, a proven significant and reliable tumor marker, especially for gastrointestinal stromal tumors and head and neck squamous cell carcinoma.[24,25] The TMEM16A channel is also considered as a novel target for cancer treatment.[26,27] This system is a member of the TMEM16 family, including 10 eukaryotic transmembrane proteins (TMEM16A-K). Despite the highly similar sequences, TMEM16 proteins present significantly different functions.[28,29] For instance, TMEM16A and TMEM16B are Ca^{2+}-activated chloride channels that enable chloride ions to conduct across the plasma membrane.[30,31] On the other hand, TMEM16C, D, G, J, and K belong to Ca^{2+}-activated lipid scramblases with a nonselective ion channel activity.[32,33] According to the structures captured by cryo-electron microscopy (cryo-EM), the difference between TMEM16 channels and scramblases is the different conformations of α-helices in the subunit cavity.[34,35]

TMEM16A is a transmembrane homodimer activated by the increase of Ca^{2+} concentration (Figure 1).[30,36] Each monomer contains one pore formed by the $\alpha 3-\alpha 7$ helix (Figure 1B), which transfers chloride ions across the membrane during the activation.[35,37,38] The pore in each monomer is independent of the activation and ion conduction.[39,40] Unlike TMEM16 scramblases, the $\alpha 4$ helix of TMEM16A rearranges to contact with the $\alpha 6$ helix on the opposite edge and construct the ion conduction pore shielded from the membrane.[37] The pore is hourglass-shaped with two wide vestibules and a narrow neck region (Figure 1B).[37] Chloride ions can pass through the narrow neck, where charge neutrality is compensated by the positively charged residues in the extracellular or intracellular vestibule.[35,41,42] The anion conduction of TMEM16A is associated with various important physiological functions, such as the secretion of various types of the exocrine gland, contraction and myogenic tone of vascular smooth muscle cells, rhythmic movements of the gastrointestinal system, airway and exocrine gland secretion, sensory transduction, and neuronal signaling.[43−45] The dysfunction of TMEM16A is

https://doi.org/10.1021/jacs.3c11940
J. Am. Chem. Soc. 2024, 146, 4665−4679

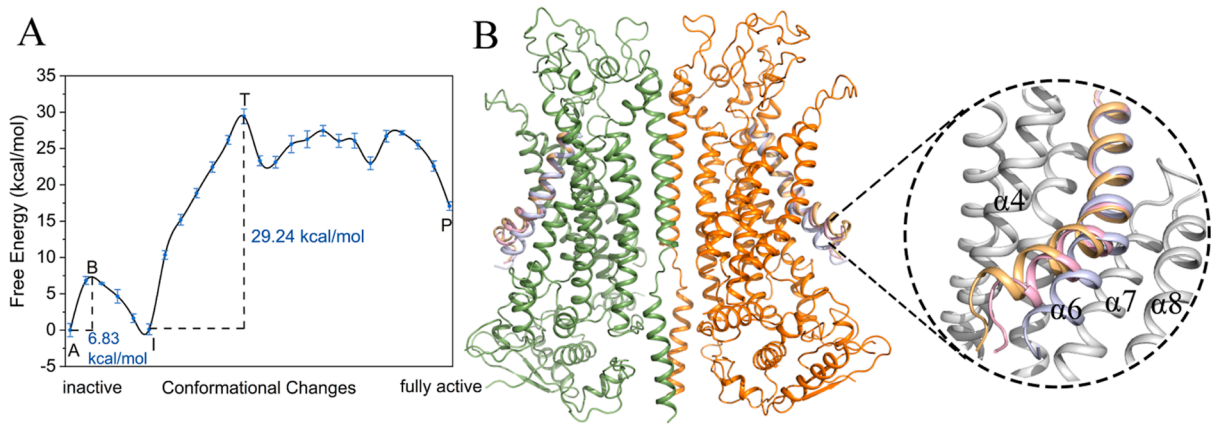

Figure 2. (A) Activation free energy profile of the TMEM16A channel. Point A is the inactive state, while point B is the transition state with a small barrier. I, T, and P, respectively, represent the intermediate, transition, and product states. The free energy of the initial state (point A) is corrected to 0. Error bars are colored blue. Conformational changes in the *X*-axis are the ones used directly from targeted MD as described by equation S6 in the Supporting Information and based on the RMSD values. There are equally spaced structural changes for the *X*-axis. (B) Superimposed structures of the TMEM16A channel, where the orientation of the $\alpha 6$ helix in the I (light orange), T (pink), and P (light blue) states is indicated. Two subunits of TMEM16A are separately colored green and orange.

related to hypertension, gastrointestinal dysfunction, cystic fibrosis, neuropathic pain, and various cancers.[46,47] Therefore, TMEM16A is considered as a potential therapeutic target for a large group of diseases.[47,48] Hence, for drug design and the treatment of these diseases, it is significant to further understand the mechanism of Ca^{2+}-activated chloride conduction of the TMEM16A channel.

Experimental studies revealed that TMEM16A is activated by the binding of two Ca^{2+} ions to the conserved site close to the anion conduction path.[39,40] The binding of two Ca^{2+} ions to a site, surrounded by five acidic residues (E654, E702, E705, E734, and D738), alters the electrostatic distributions of the intracellular vestibule and triggers the conformational rearrangement of the inner half of the $\alpha 6$ helix.[34,41] As is depicted in Figure 1C, the binding of Ca^{2+} initiates the conformational changes of the $\alpha 6$ helix and its movement toward $\alpha 7-\alpha 8$ helices.[37] The movement of $\alpha 6$ is coupled to the gate expansion in the neck region, thereby opening the gate to allow chloride conduction.[34,49] However, some details are still lacking for the activation and chloride conduction processes. For example, how does the conformational change couple to chloride conduction and when does the Cl-ion pass through the neck region are two important questions. On the other hand, some residues show strong mutational effects in moderating the activity of TMEM16A. For instance, experiments using site-directed mutagenesis revealed that some residues ($\alpha 4$ helix: I550 and I551, $\alpha 5$ helix: K588, $\alpha 6$ helix: I641, G644, K645, and E654) play an important role in the activation process (Figure S1).[34,37,41,50] However, the structural and energetic basis for these mutations is poorly understood. Moreover, there are other potential mutational sites that were not investigated but could show important impacts on the behavior of TMEM16A.

Another difficulty in investigating large biophysical systems is associated with computational cost. The size and complexity of large systems (usually containing thousands of amino acids) lead to serious computational limitations of the all-atom model. Thus, it is beneficial to use a consistent coarse-grained (CG) model[51−53] to obtain the transition state and reaction barrier. The CG model has been successfully applied to various types of systems, for instance, β_2AR,[54] ATPase,[55] myosin,[56] and Hv1 channels.[57] Note that with the CG model, we successfully predicted that the N501 mutant of the SARS-Cov2 spike protein increased the binding affinity to the ACE2 receptor in June 2020.[58] The mutant was found to contain the UK mutant (SARS-CoV-2 VOC 202012/01) and South Africa variant (501Y.V2) in December 2020. In particular, our CG model can properly describe the electrostatic term that usually contributes the most to biophysical systems.[54,55] The electrostatic-based CG model is also effective for investigating functional mechanisms in other systems.[54−56]

In this work, we combine our CG model with other techniques to investigate the functional mechanism of the TMEM16A channel. Specifically, we obtained the free energy landscape of the overall Ca^{2+}-activated chloride conduction process and located the minimal energy path and the exact time point of the chloride conduction. Furthermore, the landscape identified the critical kinetic information, including the transition state structure, reaction barrier, free energy change, and rate-determining step. Then, this information is utilized to calculate the barrier changes by mutating 57 residues of the two vestibules, the Ca^{2+} binding site, and the neck region. Finally, we explain the energy basis for the experimental mutational effects and predict 18 new mutational sites that affect the Ca^{2+}-activated chloride conduction process. Our predictions are further validated through electrophysiological experiments and proved to have superior performance. Overall, this work validates a methodology that could be applied to other biophysical systems and will contribute to the better insights on functional mechanisms of ion channels.

2. RESULTS AND DISCUSSION

2.1. Mechanism of Ca^{2+}-Activated Chloride Conduction of the TMEM16A Channel. *2.1.1. CG Free Energy Profile for Conformational Change.* The Cryo-EM structures of the TMEM16A channel (PDB ID: 5OYG and 7B5C)[34,37] provide structural details of the two end points: inactive and fully active states (Figure 1). In this study, we utilized the two structures to model the end point states and rebuild missing residues of the structure by Modeler.[59−61] Subsequently, a series of intermediate structures between the end point states were generated using targeted molecular dynamics (TMD).[62]

https://doi.org/10.1021/jacs.3c11940
J. Am. Chem. Soc. 2024, 146, 4665−4679

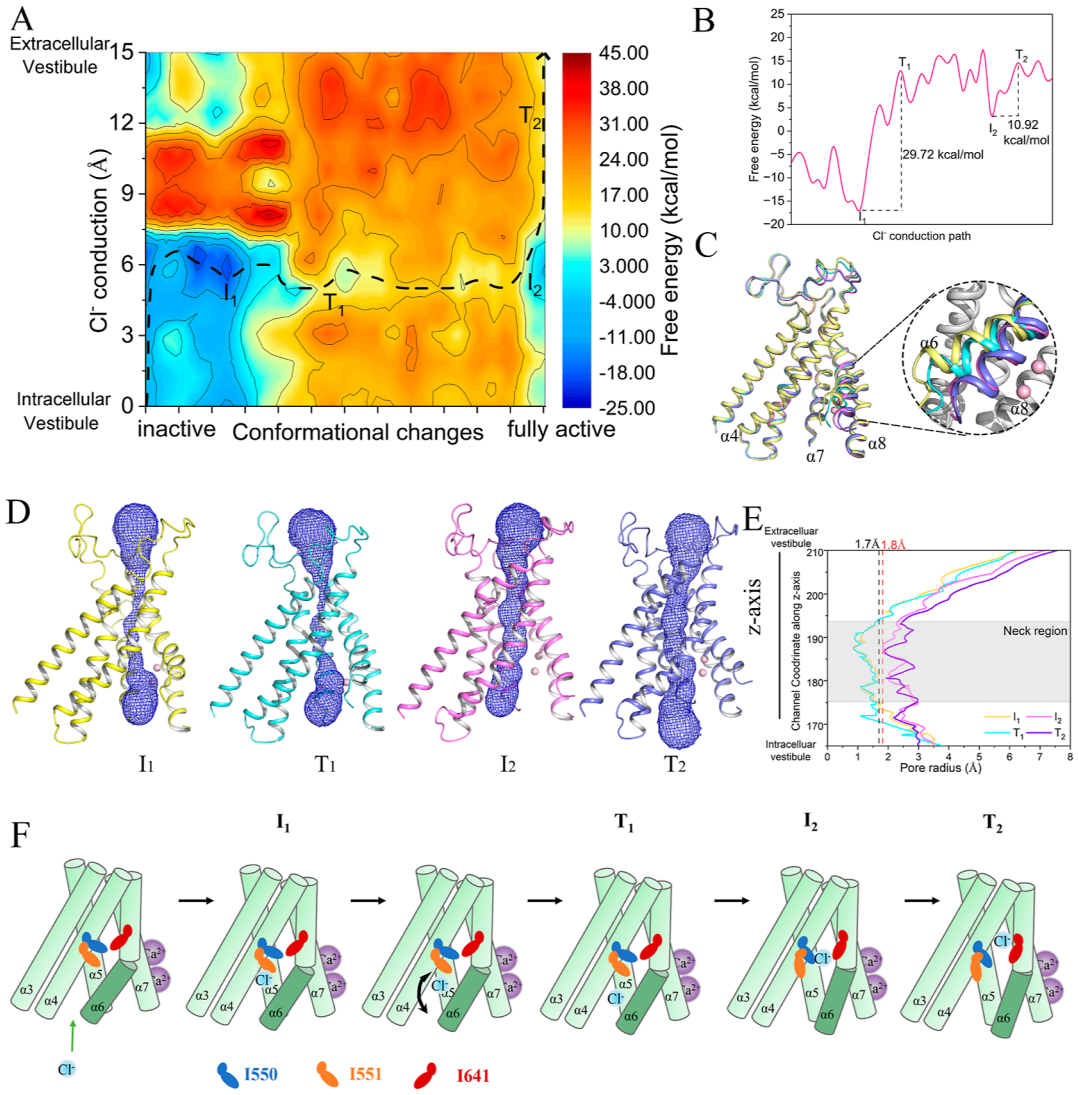

Figure 3. (A) Coupled free energy landscape of the protein conformational change and chloride conduction. The possible minimal energy path is shown by a black dashed line. The barrier along the route I_1-T_1 is 29.72 kcal/mol, while along I_2-T_2, it is 10.92 kcal/mol. Conformational changes in the *X*-axis are the ones used directly from targeted MD as described by eq S6 in the Supporting Information and based on the RMSD values. There are equally spaced structural changes for the *X*-axis. (B) Free energy profile along the minimal energy path in panel (A). (C) Comparison of the four structures in the I_1 (yellow), T_1 (cyan), I_2 (magenta), and T_2 (blue) states. Two Ca^{2+} ions are shown by pink spheres. (D) Schematic of the channel pore in the I_1 (yellow), T_1 (cyan), I_2 (magenta), and T_2 (blue) states. The blue mesh represents the Cl^- ion entry path through the vestibule region. (E) Pore radius of the channel along the *z*-axis. Two dashed lines indicate the range of the chloride ion radius (1.7−1.8 Å). The gray part represents the neck region of the channel. (F) Schematic depiction of the coupling of conformational change and chloride conduction in different steps.

For the conformational transition from the inactive to the active state, 25 intermediate structures at equal intervals were generated to calculate the free energy profiles illustrated in Figure 2 (more details are shown in the Supporting Information).

A small barrier (6.83 kcal/mol) exists from point A to B. Comparing the structures of the two points and calculating the contribution of each residue to the overall barrier (Figure S2) reveal that the residues R373 and R399 that make significant positive contributions to the A−B barrier are located in the loop connecting helixes $\alpha1$ and $\alpha2$ embedded in the membrane environment. This finding indicates that the A−B barrier may be induced by the early stage conformational change that could lead to further structural conversion.

From state B, the free energy curve goes down until the I state. The highest barrier occurs from state I to state T (29.24 kcal/mol), which is the rate-determining step of the conformational change process. Figure 2B depicts the conformational differences of the $\alpha6$ helix between the I, T, and P states. From I to T to P, the inner half of the $\alpha6$ helix undergoes the most pronounced conformational changes. It moves toward $\alpha7$ and $\alpha8$ while away from $\alpha4$. The movement proceeds with the transition of the $\alpha6$ helix into a straightened helix conformation, during which the narrow neck of the channel gradually opens. Additionally, from an energetic perspective, we also found that R461 (located in the short helix between the $\alpha2$ and $\alpha3$ helixes) and D554 (located in the $\alpha4$ helix) make the most positive contributions to the I−T barrier (Figure S3A,C). From state T to state P, the free energy decreases (Figure 2A). R461 and K583 make the most positive contributions to state T and state P (Figure S3B,D). We could suggest that these residues, especially D554 and K583 (located

https://doi.org/10.1021/jacs.3c11940
J. Am. Chem. Soc. 2024, 146, 4665−4679

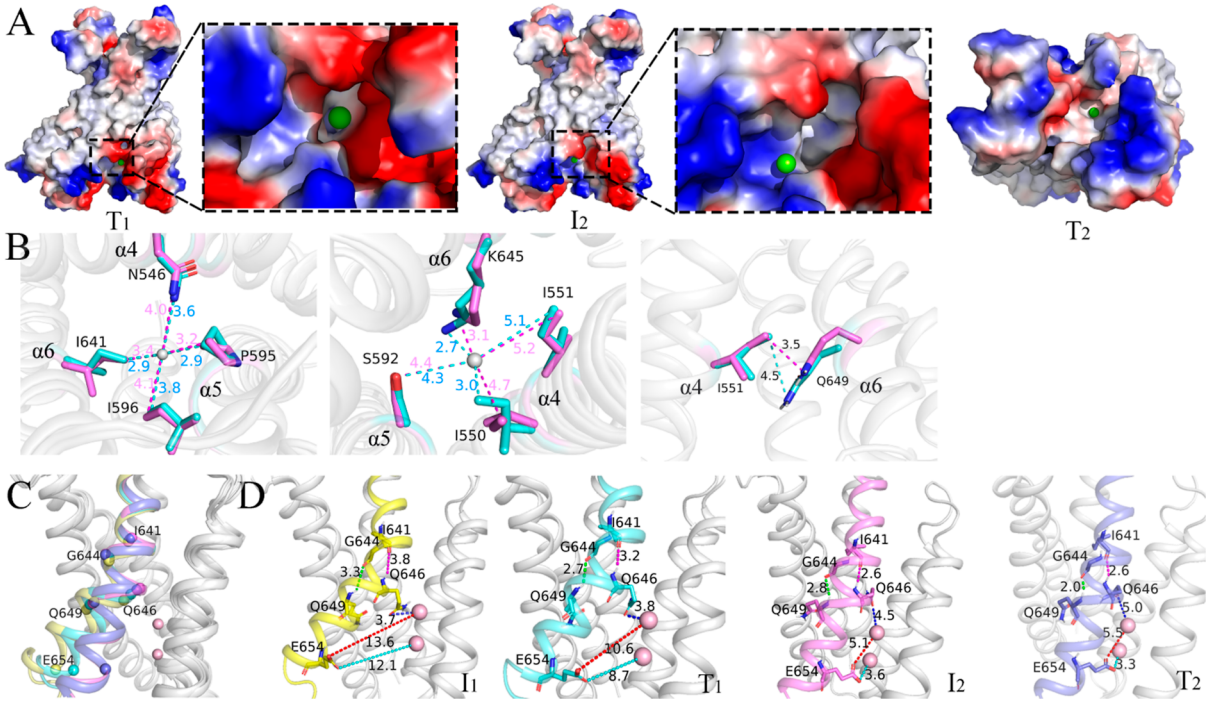

Figure 4. (A) Representation of the electrostatic potential surface in the T_1, I_2, and T_2 states. The positively charged region is colored blue, and the negatively charged region is colored red. The Cl^- ion is shown as a green sphere. (B) Top view of the distances between the center of the channel pore and the important pore-lining residues in the neck region of the T_1 (cyan) and I_2 (magenta) states (left and middle panels); distances between I551 and Q649 of the T_1 (cyan) and I_2 (magenta) states (right panel). The gray sphere represents the center of mass (COM) of Cα atoms of the four pore-lining residues. Here, we separately calculated the distances between the ND2 atom of N546, CD1 atom of I550, CD1 atom of I551, OG atom of S592, C_β atom of P595, CD1 atom of I596, CD1 atom of I641, NZ atom of K645, and the center of the pore, which is defined by the COM of Cα atoms of the four pore-lining residues (N546, P595, I596, and I641 in the left panel, I550, I551, S592, and K645 in the middle panel). The cyan and magenta dashed lines represent the distance between the COM (Cα atoms of the four pore-lining residues N546, P595, I596, and I641 in the left panel, I550, I551, S592, and K645 in the middle panel) and the residues of the T_1 and I_2 states, respectively. Distances in the I_2 state (magenta) are larger than those in the T_1 state (cyan). The main chain and hydrogen atoms of the residues are hidden for clarity. (C) Comparison of the conformations of the α6 helix in the I_1 (yellow), T_1 (cyan), I_2 (magenta), and T_2 (blue) states. The spheres in the helix represent the Cα atoms of I641, G644, Q646, Q649, and E654. Two Ca^{2+} ions are shown by pink spheres. (D) Formation of a π-helix during the conformational changes of the α6 helix. The dashed lines show the calculated distance between important residues, including the O atom of I641, N atom of Q646 (colored magenta), O atom of G644, N atom of Q649 (colored green), or residue-Ca^{2+}, including the OE1 atom of E654-Ca^{2+} (colored red), OE2 atom of E654, and Ca^{2+} (colored cyan) and OE1 atom of Q646 and Ca^{2+} (colored blue).

in helix α5) located in the Cl^- channel pore, contribute most to the conformational transition from state I to T to P.

2.1.2. Coupling between the Conformational Change and Chloride Conduction. An important issue that we try to resolve is the nature of the state where the Cl^- ion can be transduced through the channel. Experimental studies indicate that ion conduction should happen during channel pore opening, but the exact time point along the reaction coordinate is still unclear.[34,49] To explore the details of the whole process of Ca^{2+}-activated chloride conduction, we generated the chloride conduction vs conformational change free energy landscape by docking a Cl^- ion at the different positions in the channel pore of each protein conformation of Figure 2A. For each combination of the intermediate conformation obtained by TMD and the Cl^- ion, we first performed extensive MD relaxation and utilized PDLD/S-LRA/β method to calculate the binding free energy of the ion. The same approach has been used before in related studies of ion channels[63] (more details are shown in Methods Section).

As shown in Figure 3A, the free energy landscape couples the conformational change and chloride conduction, the process that corresponds to Figure 1C. The *X*-axis is the conformational change (reaction coordinate), while the *Y*-axis represents the position of chloride ions from the intracellular vestibule to the extracellular vestibule of the channel. The minimal energy path was identified and depicted by the black dashed line. We also noted that once the system reached point I_2, the narrow pore of the channel can allow chloride conduction from the intracellular vestibule to the extracellular vestibule (Figure 3A, Movies 1 and 2). There are two barriers to this path (Figure 3B). From I_1 to T_1, the barrier is 29.72 kcal/mol, which is mainly related to conformational changes (Tables S1,S2). This high barrier is the rate-determining step of the whole process of Ca^{2+}-activated chloride conduction in this work. The binding of Ca^{2+} is a key factor, which leads to channel activation, pore opening, and chloride conduction. This process was not considered explicitly in this work and may lead to the overestimated activation free energy barrier. In addition, other factors, such as the ENZYMIX force field, CG model, and implicit solvent used in our calculations, might be also related to the overestimated energy barrier. The energy barriers in other ion channels, such as TRPV4 and BEST1, are significant, of ~18 and ~24 kcal/mol.[64,65] Our simulation results provides the upper limit of the barrier. From the structural perspective, the channel undergoes pronounced conformational transitions, especially for the α6 helix. From I_1 to T_1, the electrostatic interactions make the major contributions to the energy barrier by ~37 kcal/mol (Table

https://doi.org/10.1021/jacs.3c11940
J. Am. Chem. Soc. 2024, 146, 4665−4679

S1), which indicates that the electrostatic interactions decrease a lot in the transition state T_1, thus decreasing the stability of the channel. These intrinsic changes may cause a higher energy barrier. Another barrier occurs from I_2 to T_2, 10.92 kcal/mol. The corresponding energy analysis reveals that the binding free energy of the Cl^- ion makes the major contribution to this small barrier (Table S2). It is noted that states I_1, T_1, and T_2 for combined conformational transitions and Cl^- conduction in Figure 3 are related to states I, T, and P for conformational transitions in Figure 2.

As depicted in Figure 3C, the four structures of points I_1, T_1, I_2, and T_2 are superimposed. From I_1 (yellow) to I_2 (magenta), we observed a pronounced conformational difference at the intracellular half of the α6 helix, where it has moved toward the α7 and α8 helixes (the Ca^{2+} binding sites) but away from the α4 helix. However, from I_2 (magenta) to T_2 (blue), there was no significant conformational change of the α6 helix. The free energy analysis (Figure 3A, Tables S1,S2) indicates that the movement of Cl^- ions makes the major contribution, instead of the conformational changes, during the process from I_2 (magenta) to T_2 (blue).

To further investigate the details of channel pore opening, we measured the pore radius of the I_1, T_1, I_2, and T_2 states by the HOLE program[66] (Figure 3D,E). The pore radius of the neck region of I_1 and T_1 is less than the Cl^- radius (~1.7−1.8 Å), which blocks the chloride conduction pathway. The radius of the narrowest part is ~1 Å, which is consistent with the simulation results of An's work.[67] For the I_2 (magenta) and T_2 (blue) states, the radius of the narrowest part is over 1.8 Å. These findings highlight that the neck region of the I_2 and T_2 states is open and allows for chloride conduction through the pore.

Paulino et al. revealed that the electrostatic environment at the intracellular vestibule provides the barrier for anion conduction.[37] Our findings on the electrostatic potential distribution also support this point. Besides, we found that the Cl^- ion in the T_1 state is in a strongly negatively charged environment formed by Ca^{2+} binding sites[37,41,68] (Figure 4A). The electrostatic repulsion of the Cl^- ion and the negatively charged environment hinder the movement of anions. This corresponds to the reaction barrier of 29.72 kcal/mol from I_1 to T_1, which is the rate-determining step of the whole process of Ca^{2+}-activated chloride conduction in Figure 3A,B. From T_1 to open state I_2, we observed that the Cl^- ion moves close to the positively charged region of the intracellular vestibule, which can stabilize the Cl^- ion by electrostatic attraction. As the crystallographic experiments indicate, the intracellular vestibule confers the positively electrostatic environment and lowers the energy barrier for anion conduction.[37] Our results also found that the free energy reduces from T_1 to the open state I_2 (Figure 3B), which suggests that I_2 is a stable state. When the Cl^- ion reaches T_2, the anion is surrounded by a local negatively electrostatic environment that is mainly induced by pore-lining E624 (located in the loop connecting α5 and α6 helixes) and E633 (located in the α6 helix) in the extracellular vestibule (Figure S4), despite the extracellular vestibule mainly providing a positively electrostatic environment that makes favorable contributions to chloride conduction.[37,68] The changes in electrostatic environments for chloride conduction from I_2 to T_2 account for the small barrier of I_2−T_2 in Figure 3B.

In order to further investigate the conformational changes of the neck region, we focused on the pore-lining residues (α4 helix: N546, I550, and I551, α5 helix: S592, P595, and I596, α6 helix: I641, K645, and Q649) around the neck region (Figure S5) of T_1 (cyan) and I_2 (magenta). We measured the distance between the center of the channel pore and the pore-lining residues (Figure 4B). Our findings indicate that the distances of the I_2 state (magenta) are larger than those of the T_1 state (cyan) (Figure 4B and Table S3). Overall, the pore formed by the key residues lining the channel of the neck region in the I_2 state (magenta) is larger than that in the T_1 state (cyan). It also suggests that from T_1 (cyan) to I_2 (magenta), the neck region is opening. The opened gate allows Cl^- ions to pass through the neck region (Figure 3F, Movies 1 and 2). Specifically, we monitored the distance between I551 and Q649, and the interaction was argued to have the capability to stabilize the open pore.[49] According to our result, from T_1 to I_2, the distance of I551−Q649 reduced from 4.5 to 3.5 Å (Figure 4B), which validates the stabilizing effect.

The experimental results suggest that activation and pore opening can proceed with the transition of the inner half of the α6 helix from loose conformation (α6 helix either mobile and disengaged as found in the Ca^{2+}-free structure of the channel) to a strained π-helix (rigid α6 helix in contact with the binding site as displayed in the Ca^{2+}-bound structure).[37,49] We monitored the movements of the inner half of α6 to reveal more details of the π-helix formation (Figure 4C,D) and found that accompanied by the conformational transition in the process of channel activation, the distances of I641−Q646, G644−Q649, and E654−Ca^{2+} gradually decrease. Conversely, the distance of Q646−Ca^{2+} increases. These results indicate that during activation, the inner half of helix α6 moves toward Ca^{2+} (Movie 2). The negatively charged E654 in the terminal of helix α6 gets close to the two Ca^{2+} ions due to electrostatic attraction. The movement can propagate upward and promote the movement of Q646 toward I641, away from Ca^{2+} and induce the distance changes of G644−Q649. These motions generate the straightened conformation of the α6 helix, accompanied by the formation of the π-helix (Movie 2).

2.2. Predicting Mutational Effects Based on Barrier Analysis. According to the above analysis, we have elucidated the mechanism of Ca^{2+}-activated chloride conduction of the TMEM16A channel and obtained the kinetic information, especially the reaction barrier and the transition state structure. The information was utilized to evaluate the mutational effects on the barrier change in this work, which determines the speed and effectiveness of the activation process according to the rate theory (see the computational details in the Methods Section). Moreover, we focused on the directions (inhibiting or facilitating the function of Ca^{2+}-activated chloride conduction) and the strength of the mutational effects.

Experimental studies indicate that the binding of two Ca^{2+} ions triggered the activation of TMEM16A.[37] Two highly hydrophilic vestibules confer a positive electrostatic environment throughout the pore and facilitate chloride conduction.[37] Besides, Lam et al. found that a hydrophobic gate at the intracellular entrance of the channel neck affected chloride conduction and determined that three residues (I550, I551, and I641) formed the key hydrophobic gate, which stabilized the gate in the closed channel pore by mutagenesis.[34,49]

Our initial effort was aimed at investigating whether other residues on the two vestibules, Ca^{2+} binding sites, or the neck region could affect Ca^{2+}-activated chloride conduction by mutating to Ala. The corresponding results of the mutational

https://doi.org/10.1021/jacs.3c11940
J. Am. Chem. Soc. 2024, 146, 4665−4679

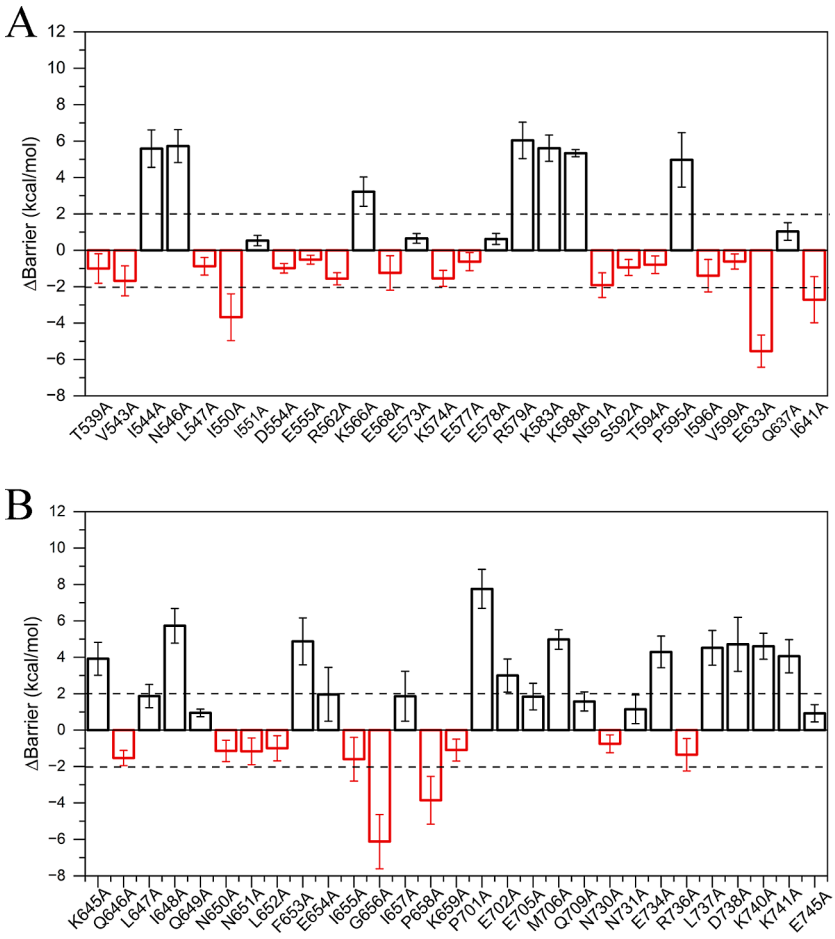

Figure 5. Evaluation of mutational effects of the residues on the two vestibules, Ca^{2+} binding sites, and pore-lining neck region. The effects were calculated using ΔBarrier = $Barrier_{mutant}$ − $Barrier_{WT}$. ΔBarrier > 0 (shown as black bars) indicates that the mutation impedes ion conduction, and ΔBarrier < 0 (shown as red bars) indicates that the mutation facilitates ion conduction. The black dash lines distinguish the mutations with |ΔBarrier| ≥ 2 kcal/mol. The data are expressed as means ± SEM.

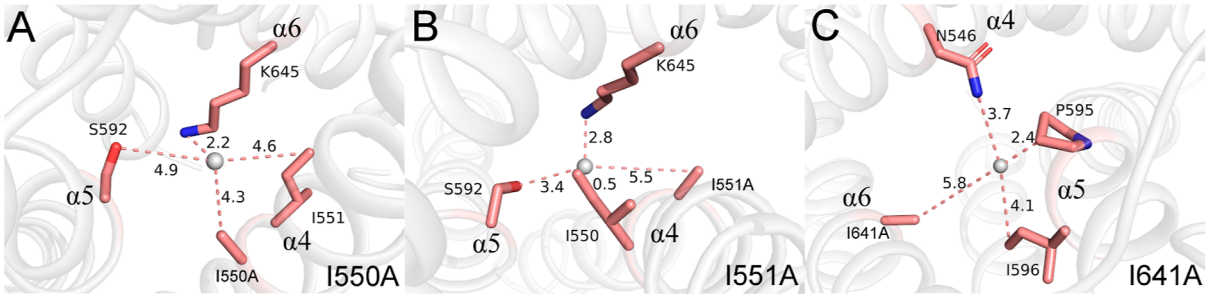

Figure 6. Explanation of mutational effects of I550A, I551A, I641A, and Q649A. (A–C) Top view of the distances between the center of the channel pore and the important pore-lining residues in the neck region. The gray sphere represents the COM of the Cα atoms of the four pore-lining residues. The salmon dashed lines represent the distance between COM and the pore-lining residues. The main chain and hydrogen atoms of the residues are hidden for clarity.

effects are illustrated in Figure 5. Moreover, we calculated the change of energy barrier between each mutant and wild type (ΔBarrier = $Barrier_{mutant}$ − $Barrier_{WT}$, more details are shown in the Methods Section). ΔBarrier > 0 indicates that the mutation leads to a higher energy barrier and inhibits chloride conduction. ΔBarrier < 0 indicates that the mutation reduces the barrier and facilitates chloride conduction. Additionally, I550A and I641A show an obvious decrease in the energy barrier, facilitating chloride conduction. I551A and Q649A show a slight increase in the energy barrier, inhibiting chloride conduction. These calculations are encouragingly consistent with the results of the electrophysiological experiments by Lam et al.[34,49] Indeed, the authors observed that I550A and I641A increase the single-channel conductance, while I551A and Q649A decrease the single-channel conductance.[49]

According to the structural analysis of the mutations (I550A, I551A, I641A, and Q649A) in the transition state (Figures 6 and S6), we found that for I550A, the sum of distances between the center of the channel pore and the four pore-lining residues (I550A, I551, S592, and K645) of the neck

https://doi.org/10.1021/jacs.3c11940
J. Am. Chem. Soc. 2024, 146, 4665−4679

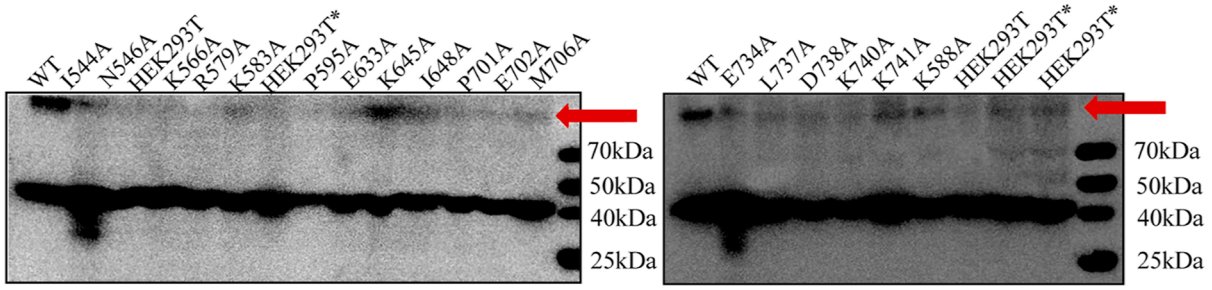

Figure 7. Western blot images of TMEM16A and its mutant forms of expression in HEK293T cells. The red arrow indicates the location of the target protein. "*" denotes duplicate samples.

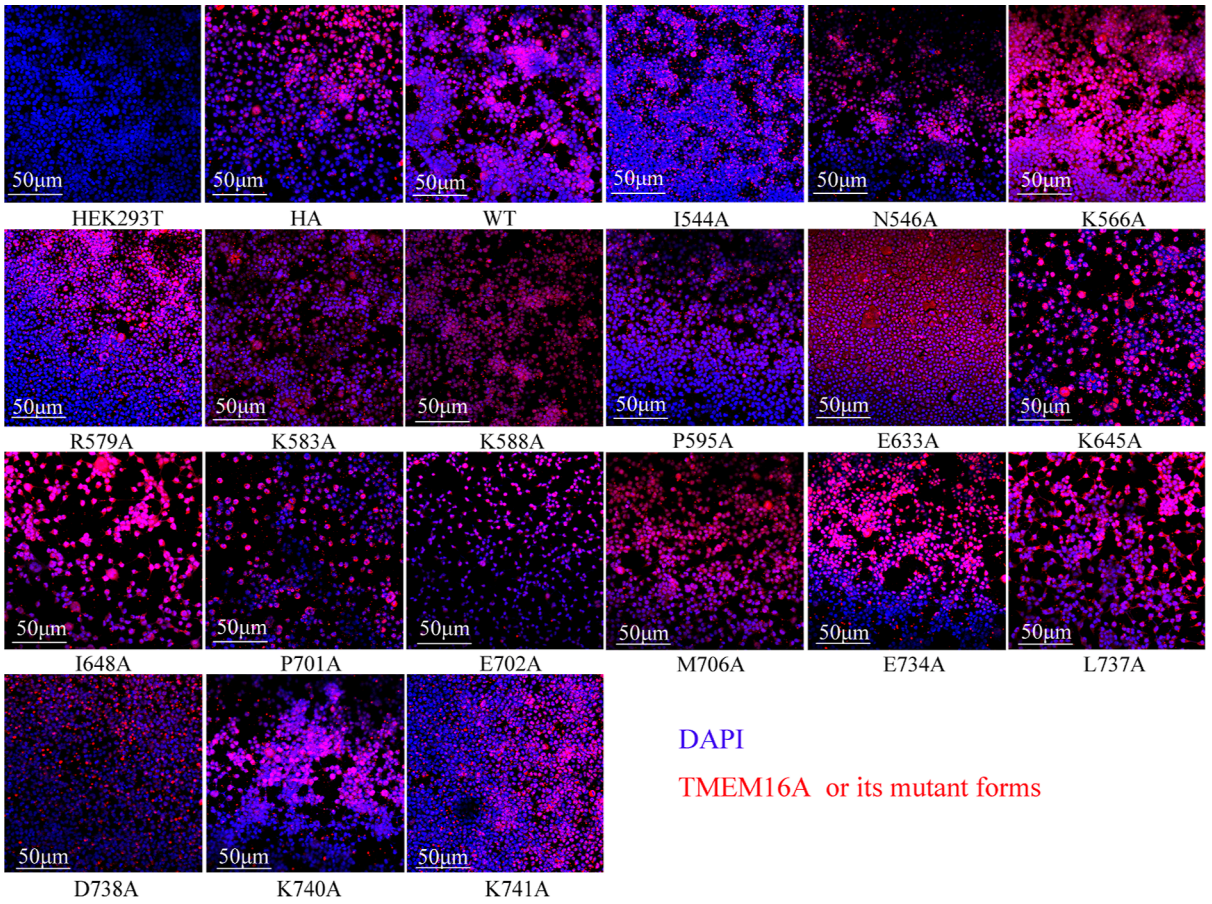

Figure 8. HEK293T cells expressing TMEM16A or its mutant forms were stained with DAPI and anti-HA antibodies and then analyzed by confocal microscopy (scale bar, 50 μm).

region is about 16 Å (Figure 6A and Table S4). Before mutation, the sum of the distances is about 15.1 Å (distances of COM-I550/I551/S592/K645 in Figure 4B and Table S4). Thus, I550A expands the channel pore in the neck region and may explain the facilitating effects on the chloride conductance. Similarly, I641A also induces the dilation of the channel pore with higher total distances of 16 Å (Figure 6C and Table S5) than 13.2 Å in the wild type (distances of COM-N546/P595/I596/I641 in Figure 4B and Table S5). This result is for a different set of distances, which had a sum of 15.1 Å in the WT channel (distances of COM-I550/I551/S592/K645 in Table S4). The dilated pore promotes the passing of Cl^- ions and increases the conductance.

Oppositely, for I551A, the sum of the distances is 10.2 Å (Figure 6B and Table S4), obviously smaller than 15.1 Å in the wild type (Figure 4B and Table S4). This suggests that this mutant constricts the narrow pore and impedes chloride conduction. This may account for the decrease in the single-channel conductance for I551A.[49] For Q649A, we calculated the distance between the Cl^- ion and Q649(A). Excluding the length difference of the side chain between Q649 and Q649A (Figure S6A), the mutation increases the distance of the Cl^- ion and Q649(A) from 9.6 to 13.0 Å (Figure S6B,C). We speculated that the mutation from the polar glutamine to the nonpolar alanine breaks the local polar interactions, which is important for anion conduction. Thus, Q649A leads to an adverse effect on chloride conduction. Besides, the interaction between I551 and Q649 can stabilize the open pore[49] and promote chloride conduction (Figure 4B). The mutation

https://doi.org/10.1021/jacs.3c11940
J. Am. Chem. Soc. 2024, 146, 4665−4679

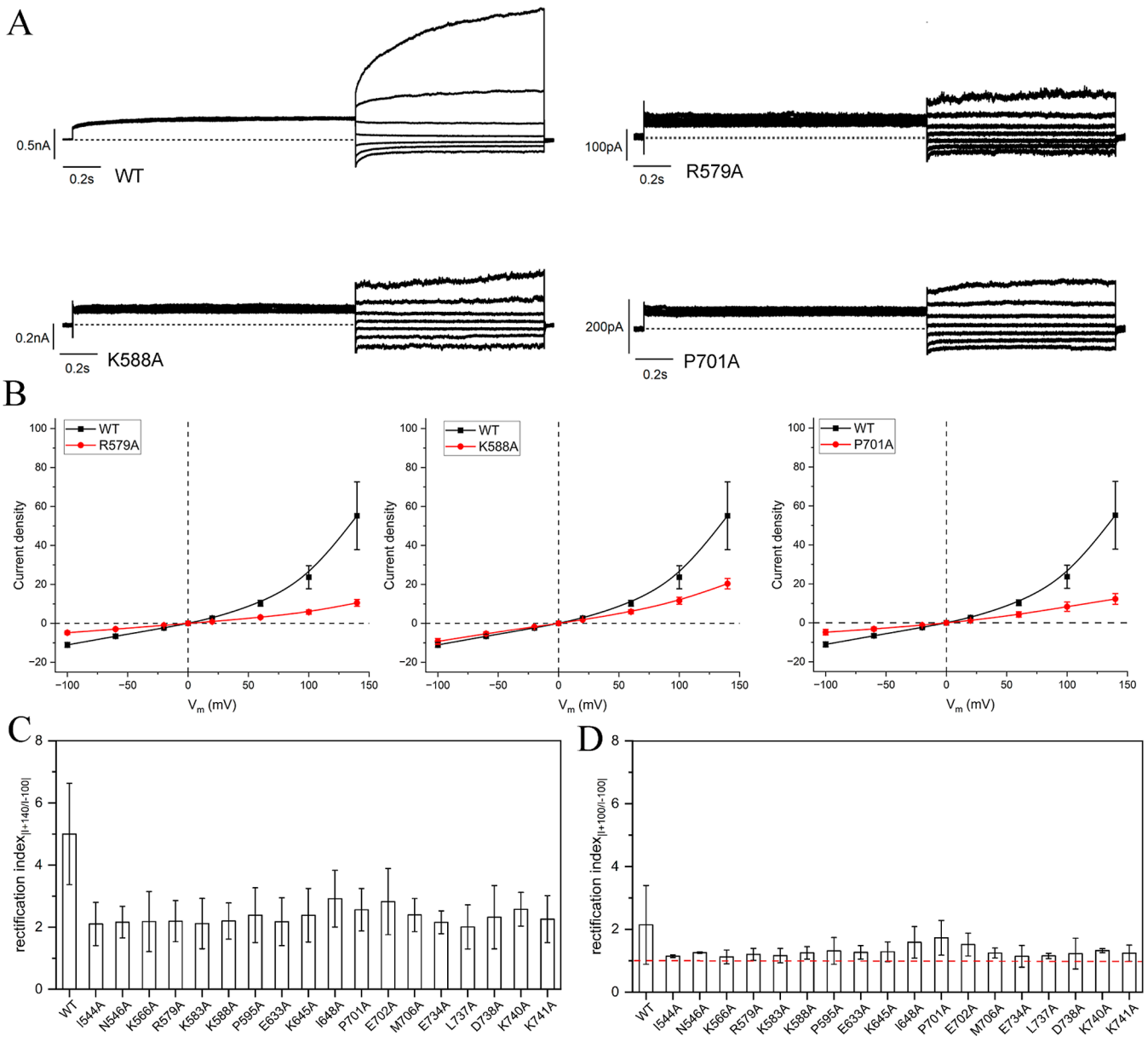

Figure 9. Electrophysiological verifications. (A) Steady-state currents for the wild type, R579A, K588A, and P701A recorded by the whole-cell currents using patch-clamp experiments after activation with 0.5 μM Ca^{2+} at a given V_m = −100 mV, −60 mV, −20 mV, +20 mV, +60 mV, +100 mV, +140 mV. The dashed horizontal lines represent the zero-current level. (B) Whole-cell current density versus V_m (I−V) relationships. The number of experiments was 5 in each case. (C,D) Rectification index ($|I_{+140}/I_{-100}|$, $|I_{+100}/I_{-100}|$) for the wild type and each mutation. All data are expressed as means ± SEM. The red dashed line represents RI = 1.

Q649A disrupts the interaction, which is unable to stabilize the open pore and impedes chloride conduction.

Additionally, based on our current analysis, we can further predict other residues that might have facilitating/inhibiting mutational effects on Ca^{2+}-activated chloride conduction other than the reported residues I550, I551, I641, and Q649. From the barrier change analysis presented in Figure 5, we found that I544A, N546A, and K566A of the α4 helix, R579A, K583A, K588A, and P595A of the α5 helix, K645A, I648A, and F653A of the α6 helix, P701A, E702A, and M706A of the α7 helix, E734A, L737A, D738A, K740A, and K741A of the α8 helix might also inhibit Ca^{2+}-activated chloride conduction, like I551A and Q649A. However, E633A, G656A, and P658A might facilitate Ca^{2+}-activated chloride conduction, like I550A and I641A.

For the positively charged residues K566, R579, K583, K588, K645, K740, and K741, the mutation to Ala breaks the positively charged electrostatic environment (Figure S7A−D). Thus, they impede the negatively charged chloride conduction through the pore. The negatively charged residues E702, E734, and D738 are in the Ca^{2+}-binding site. The electrostatic attractions between them stabilize the binding of Ca^{2+} and the rearrangement of α6 helix conformation, which helps the channel pore to remain open and allow Cl^- ions to pass through.[37,41] These mutations break the stable binding of Ca^{2+} and inhibit pore opening and chloride conduction. For E633, its mutation also breaks the electrostatic interactions in the extracellular vestibule (Figure S4). After mutation, the electrostatic repulsion between E633 and chloride ions disappeared, which facilitates chloride conduction. I544A,

https://doi.org/10.1021/jacs.3c11940
J. Am. Chem. Soc. 2024, 146, 4665−4679

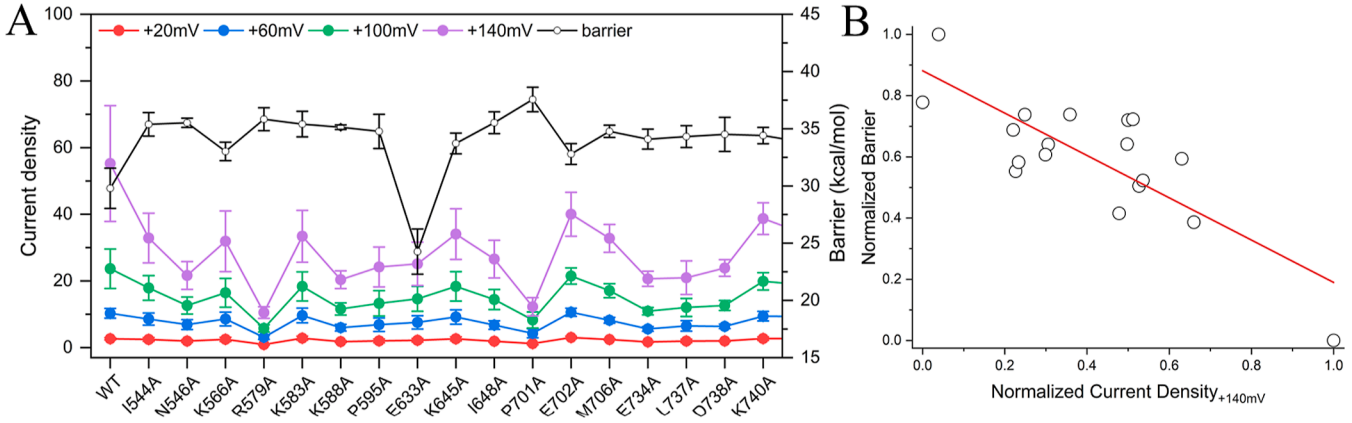

Figure 10. Comparison of the current density from electrophysiological experiments and the barriers from our computational results. (A) Comparison of the barrier from our calculations and the current density from electrophysiology. All data are expressed as means ± SEM. (B) Correlation analysis between the normalized barriers (except E633A mutant) of our calculations and the normalized current density at a given V_m = +140 mV. The red line derives from the linear fitting. The spheres represent the data.

N546A, and P595A in the neck region also reduce the pore size and impede the conduction of Cl^- ions (Figure S7E−G and Table S5). P701A, M706A, and L737A stabilize the binding of Ca^{2+} ions due to the steric hindrance from the side chains. I648 forms the interaction with G644, which plays an important role in the formation of the π-helix (Figure S7H,I). The mutation at I648 decreases the interaction and impedes the formation of the π-helix. It also affects the movement of the α6 helix, which is essential for chloride conduction. Similarly, F653A increases the distance between E654 of the α6 helix and the two Ca^{2+} ions compared to the T_1 state of the wild type (Figures 4D and S7J). It reduces the electrostatic interaction between E654 and Ca^{2+} ions and hinders the movement of the α6 helix and the formation of the π-helix. G656 and P658 are in the flexible loop of the inner terminal of the α6 helix. After mutating to Ala, the backbone of the inner half of helix α6 is closer to the Ca^{2+}-binding site (Figure S7K−L). It suggests that the mutant channel pore is more open and facilitates ion conduction.

2.3. Experimental Validation of the Computational Predicted Mutational Effects. To verify our predictions, we performed experimental studies of the effect of mutations of residues with ΔBarrier ≥ |2| kcal/mol. These verifications were performed using the patch-clamp technique. We established the cell lines for the wild type and 21 predicted mutations. To examine whether the predicted mutations of TMEM16A were expressed in cells, we tested for the expression of these proteins by Western blotting and found that these mutant proteins were expressed successfully in HEK293T cells except for F653A, G656A, and P658A (Figure 7). Moreover, the immunostaining assay observed obvious red fluorescence signals in HEK293T cells expressing TMEM16A or its mutant forms (Figure 8). These data suggest that TMEM16A or its mutant forms can be expressed successfully in HEK293T cells. However, the failure of the cell culture for F653A, G656A, and P658A makes it impossible to perform functional experimental verifications for those mutants. Finally, we carried out the patch-clamp experimental verifications for the wild type and 18 mutations.

The steady-state currents were recorded by the whole-cell currents by patch-clamp experiments after activation with 0.5 μM Ca^{2+} at a given V_m = −100 mV, −60 mV, −20 mV, +20 mV, +60 mV, +100 mV, +140 mV[42] (Figures 9A and S8). Note that the current in the wild type is stronger than that in all mutations. The mutational effects can be reflected by the current density. Besides, we obtained the current density for all cell lines according to the current and cell capacitance at different V_m. As shown in Figures 9B and S9, we compare the $I-V$ relations for each mutant and wild type. The curves indicate that overall, the current density of 18 mutants is weaker than that of the wild type at different V_m. This finding suggests that these mutants impede chloride conduction in the channel pore, which is consistent with our predicted mutational directions except for E633A (Figure 5). Hence, the accuracy of our predictions on the mutational effects on the directions is about 94%. We speculated that for E633, its mutation breaks the electrostatic repulsion between E633 and chloride ions (Figure S4). The electrostatic repulsion facilitates the release of Cl^-. Thus, the E633A mutant reduced experimental Cl^- current density as other mutants tested.

To evaluate the magnitude of the $I-V$ curve rectification, the index of rectification (RI) is quantified as the ratio of the absolute current density measured at +140 mV (I_{+140}) and −100 mV (I_{-100}) (RI = $|I_{+140}/I_{-100}|$) in the presence of 0.5 μM Ca^{2+}. Therefore, RI of the linear $I-V$ is close to 1. RI > 1 represents outwardly rectified $I-V$ curves, while RI < 1 represents inwardly rectified $I-V$ curves. The extent of inward or outward rectification is indicated by the deviation of RI from 1. For the wild type and all mutants, the values of RI are more than 1 (Figure 9C), which indicates the outwardly rectifying relationship between the steady-state current density and the V_m. For all mutants, RI is lower than for the wild type, which has an RI of 5.0. It shows that the rectification degree of the wild type is larger than that of the mutants. We also measured the rectification index at +100 and −100 mV (Figure 9D). Similarly, for the wild type and all mutants, the values of $RI_{|I+100/I-100|}$ are all more than 1, indicating the outwardly rectifying relationship of the $I-V$ curves. Additionally, due to the highest $RI_{|I-100/I+100|}$ in the wild type, the rectification degree of the wild type is larger than that of the mutants.

Figure 10A depicts the current density of the wild type and the mutants at a given V_m = +20 mV, +60 mV, +100 mV, +140 mV. Our findings indicate that the current density of each mutation reduces much more than the wild type. This suggests that the anion conductance function of the TMEM16A channel is inhibited for these mutants. When the given V_m increases, the current density of the wild type and all mutants

https://doi.org/10.1021/jacs.3c11940
J. Am. Chem. Soc. 2024, 146, 4665−4679

has the same increasing tendency. Additionally, Figure 10A also describes the curve of the computed free energy barriers for chloride conduction. In principle, a higher barrier represents a stronger inhibition of chloride conduction of the channel and corresponds to a weaker current density. In other words, a higher computed barrier should correspond to a lower current density. In this study, the trend between the current density and the barrier is as expected except for E633A. For instance, when $V_m > 0$, the current density of the wild type is the largest. The wild-type channel's barrier is the lowest in our calculations for the mutants tested experimentally. For R579A and P701A, the current density is lower. The corresponding barriers of the two mutants are higher, as expected.

To assess the predicted mutational effect strength, we performed a correlation analysis by linear fitting the normalized barriers of our calculations and the normalized current density at a given V_m = +140 mV. In this work, we normalized barriers and current densities according to the formula $X_{normalized} = \frac{(X - X_{minimum})}{(X_{maximum} - X_{minimum})}$. As depicted in Figure 10B, the barrier and current density are negatively correlated. The Pearson's correlation coefficient is −0.80, presenting a strong negative correlation between our predictions and electrophysiological results. It indicates that our predictions of mutational effect strength are relatively reliable. We also compared computed free energy barriers with experimental current densities recorded at +20, +60, +100 mV (Figure S10). The barrier and current density are negatively correlated, and the Pearson's correlation coefficients are −0.59, −0.65, and −0.7, respectively. The results present a moderately negative correlation between our predictions and electrophysiological results. The moderate negative correlation may be due to lower current values. Moreover, the addition of E633A mutant causes the Pearson's correlation coefficient to drop to −0.4 (Figure S11). It seems that a weak correlation maybe due to using the minimum barrier of E633A mutant in the normalization.

3. CONCLUSIONS

Herein, we utilize a general approach based on the analysis of free energy barrier changes between the mutants and the wild type to predict the mutational effects on Ca^{2+}-activated chloride conduction of TMEM16A. Specifically, we focus on the change in the free energy barriers upon mutation. The approach has prominent advantages over static structural analysis that depends on the interaction distance and angle of the residues in the stable state. Additionally, the structural analysis ignores the transition state and reaction barriers, which play critical roles in the reaction process. Moreover, the mutational effect is affected by the overall change in energy associated with the substitution.

By studying the underlying mechanism, this work predicts the mutational effects of Ca^{2+}-activated chloride conduction of the TMEM16A channel. Crystallographic experiments captured the structures of TMEM16A channel at the inactive and the fully active states,[34,37] which paves the way for computational modeling. Our findings suggest that the channel activation of TMEM16A induces conformational changes and subsequent anion conduction. By utilizing the two end point structures (inactive and active state), we construct the transition details of the activation process, calculate the free energy profiles, and identify the transition state and the rate-determining step. Furthermore, to identify the exact time point of chloride conduction, the conformational changes are coupled with chloride conduction to generate the free energy landscape. The landscape map shows the minimal energy path, with an energy barrier of 29.72 kcal/mol.

According to the transition state and energy barrier, we assessed the mutational effects based on the change in barrier height. Previous discussions[34,67] on mutational effects rely on structural analysis, such as changes in key interactions, which mainly reflects on the changes in the distance of the key interacting residues while ignoring the role of the transition state and reaction barrier. However, sometimes the mutation may affect the overall electrostatic distribution near the site, unlike a single interaction. Hence, we establish a general approach for predicting mutational effects based on the mechanism study and barrier analysis. For I550A, I551A, I641A, and Q649A mutants, our predictions are consistent with the previous experimental results.[34,49] Nevertheless, for newly predicted residues, we validated their behavior by patch clamp experiments. Encouragingly, the high accuracy (about 94%) of mutation effect directions (inhibiting/facilitating chloride conduction) and the Pearson's correlation coefficient (about −0.8) for mutation effect strength prove the reliability of our prediction.

Although our predictions appeared to be consistent with the patch clamp experiments, the free energy barrier seems to be overestimated in our calculations. The overestimation may be related to the unconsidered Ca^{2+} binding process and the limitation of the CG energy calculations used. At any rate, the predictions are quite reasonable. In terms of computational speed in our CG method, we can quickly predict possible mutational effects.

Overall, this work elucidates the mechanism of Ca^{2+}-activated chloride conduction of TMEM16A and emphasizes a general approach for predicting mutational effects by barrier analysis (free energy barrier changes between the mutants and wild type). The methodology is constructive to our understanding of physiological and pathophysiological processes in ion channels and useful to treat ion channel diseases caused by pathogenic mutations. Besides, the approach could be expanded to other biophysical systems.

4. METHODS

4.1. Model Preparation. We obtained the Cryo-EM structures of the Ca^{2+}-free TMEM16A (inactive state, PDB ID:5OYG[37]) and Ca^{2+}-bound TMEM16A (fully active state, PDB ID:7B5C[34]) at the 4.06 and 3.7 Å resolution from the Protein Data Bank, respectively. The two structures generated the two end point states and missing residues of the structure were rebuilt by Modeler.[59−61] Then, TMD[62] was performed on the all-atom structures of the complete homodimer to generate a series of intermediate structures and connected the two end points. After that, conformational changes from the inactive to a fully active state were constructed. Our simulations are performed by Molaris-XG package version 9.15.[69,70] The system was solvated by a surface constraint all-atom solvent[71] sphere with a radius of 40 Å. Water molecules are represented by Langevin dipoles. The surface-constrained water sphere region was surrounded by a 2 Å Langevin dipole surface. The ENZYMIX force field[52,70] was used. The long-range electrostatic effect was treated by the local reaction field method.[72] A gird of unified atoms was used to represent membrane particles and were added to the system by Molaris-XG.[52,70] Each system is composed of about 31000 atoms. For each system, energy minimization was applied, including 10000 steps of the steepest descent algorithm and 10000 steps of the conjugate gradient algorithm. Then, each system was relaxed by MD runs at 300 K, until the energy reached convergence (energy basically stops falling). The relaxation time is about 0.5 ns. Time step is 1 fs. The simulations

https://doi.org/10.1021/jacs.3c11940
J. Am. Chem. Soc. 2024, 146, 4665−4679

were performed in the *NVT* ensemble at 300 K maintained by a Langevin thermostat. After that, these structures were trimmed into CG models (~21000 atoms in each model), the protonation states of each residue are determined by Monte Carlo proton transfer (MCPT) algorithm;[52] another relaxation run is performed (time step 1 fs, simulation time 1 ns) before evaluating the CG free energy profiles of the conformational changes in the activation process.

For chloride conduction coordinates, we utilized Molaris-XG[69,70] to build the all-atom model by docking chloride ions at the different positions of the channel pore for each intermediate structure. From the intracellular vestibule to the extracellular vestibule, chloride ions were positioned every 2 Å in the z direction along the channel pore. In total, for each intermediate structure, a chloride ion was positioned at 16 different z values along the channel pore to represent its conduction. Due to independence of the activation and ion conduction in each subunit,[39,40] the ion conduction process was only studied for the right subunit in this work. Subsequently, extensive MD relaxation was implemented using Molaris-XG for 0.5 ns at 300 K maintained by the Langevin thermostat, until the energy reached convergence (the energy basically stops falling). We calculated the binding free energies of these structures and combined the data with the CG free energy profiles to obtain the free energy landscape of the Ca^{2+}-activated chloride conduction.

4.2. Free Energy Profiles by CG Simulations. Our developed CG model[51,52] evaluated the free energy profiles. The model emphasizes an accurate description of the electrostatic interactions in proteins and the solvation of the ionizable residues. Specifically, we converted the all-atom structures (the intermediate structures generated by TMD) into CG models, where the side chain of the residue is trimmed into a simplified united atom. Next, we performed extensive MD relaxation at 300 K, until the energy reached convergence (energy basically stops falling). The relaxation time is about 0.5 ns. Time step is 1 fs. We determined the protonation state of the ionizable residues by the MCPT algorithm.[52] MCPT was implemented in the proton transfer between the ionizable residues until the electrostatic free energy of the folded protein converged. The convergence criterion for the electrostatic free energy of the folded protein is that the energy basically stops falling. Besides, the proton acceptance probability was evaluated by the standard Metropolis criterion. Based on the obtained charge distribution, we calculated the free energy of each model by CG simulations. All calculations were implemented into Molaris-XG.[69,70]

The total free energy of our CG model includes the following terms

$$\Delta G_{\text{fold}} = \Delta G_{\text{main}} + \Delta G_{\text{side}} + \Delta G_{\text{main-side}} \tag{1}$$

$$= c_1 \Delta G_{\text{side}}^{vdW} + c_2 \Delta G_{\text{solv}}^{\text{CG}} + c_3 \Delta G_{\text{HB}}^{\text{CG}} + \Delta G_{\text{side}}^{\text{elec}} + \Delta G_{\text{side}}^{\text{polar}} + \Delta G_{\text{side}}^{\text{hyd}} + \Delta G_{\text{main-side}}^{\text{elec}} + \Delta G_{\text{main-side}}^{vdW} \tag{2}$$

Each term in eq 1, respectively, represents the main-chain interaction energy, side-chain interaction energy, and interaction energy between the main chain and side chain. The terms in eq 2 are the side-chain van der Waals energy, main-chain solvation energy, main-chain hydrogen bond energy, side-chain electrostatic energy, side-chain polar energy, side-chain hydrophobic energy, electrostatic energy between the main chain and side chain, and van der Waals energy between the main chain and side chain. c_1, c_2, and c_3 represent the scaling coefficients set to 0.1, 0.25, and 0.5 adopted from the previous study.[51,52]

4.3. Binding Free Energy of Chloride Conduction by Atomistic Simulations. We calculated the binding free energy for the chloride conduction models by atomistic simulations using the PDLD/s-LRA/β method.[73−75] Additionally, the scaled protein dipole Langevin dipole (PDLD/S) is the method that evaluates the electrostatic energy of the system at a semimicroscopic level and maintains the advantages of the microscopic and macroscopic levels. In PDLD/S, considering the solvent average polarization, the grid of Langevin dipoles (LD) represents the solvent molecules. Linear response approximation (LRA) is applied to average polarization, and the linear interaction method (LIE) approximates the nonelectric binding contribution by a scaled vdW term. Therefore, the overall method was named PDLD/S-LRA/β, where β represents the scaling of the vdW term.

In this study, the PDLD/S-LRA/β calculates the binding free energy between the ion Cl^- and the TMEM16A channel. The calculations were performed using the POLARIS module in the Molaris-XG software.[70] The binding free energy is computed using the following equation

$$\Delta G_{\text{bind}}^{\text{PDLD/S-LRA}/\beta} = \Delta G_{\text{bind}}^{\text{elec}} + \beta(\langle U_{vdW,\iota}^{\text{p}} \rangle_\iota - \langle U_{vdW,\iota}^{\text{w}} \rangle_\iota) \tag{3}$$

$$\Delta G_{\text{bind}}^{\text{elec}} = \frac{1}{2}(\langle U_{\text{elec},\iota}^{\text{p}} \rangle_\iota - \langle U_{\text{elec},\iota}^{\text{w}} \rangle_\iota) + \frac{1}{2}(\langle U_{\text{elec},\iota}^{\text{p}} \rangle_{\iota'} - \langle U_{\text{elec},\iota}^{\text{w}} \rangle_{\iota'}) \tag{4}$$

where $\Delta G_{\text{bind}}^{\text{elec}}$ is the electrostatic term of the binding energy, U is the specific effective potential, and sign $\langle\ \rangle$ represents the average value. The contribution of van der Waals is scaled with $\beta = 0.25$. The superscripts p and w are the protein and water environment. ι and ι' represent the ligand with the actual charged form and the nonpolar ligand with 0 residual charge, respectively.

4.4. Mutational Effects. We evaluated the mutational effects by barrier changes between the mutants and the wild type TMEM16A channel.

For the wild type

$$\text{Barrier}_{\text{WT}} = (\Delta G_{\text{fold}} + \Delta G_{\text{bind}}^{\text{PDLD/S-LRA}/\beta})_{T_1} - (\Delta G_{\text{fold}} + \Delta G_{\text{bind}}^{\text{PDLD/S-LRA}/\beta})_{I_1} \tag{5}$$

For the mutants

$$\text{Barrier}_{\text{MT}} = (\Delta G_{\text{fold}} + \Delta G_{\text{bind}}^{\text{PDLD/S-LRA}/\beta})_{T_1} - (\Delta G_{\text{fold}} + \Delta G_{\text{bind}}^{\text{PDLD/S-LRA}/\beta})_{I_1} \tag{6}$$

The barrier changes

$$\Delta\text{Barrier} = \text{Barrier}_{\text{MT}} - \text{Barrier}_{\text{WT}} \tag{7}$$

where T_1 and I_1 are the same channel states as in Figure 3.

4.5. Cell Culture and Cell Line Established. The HEK293T cells were purchased from the American Type Culture Collection (ATCC). The cell lines were identified by short tandem repeat analysis and were guaranteed to be used within 6 months. The most recent testing was performed 3 months ago. All cell lines were maintained in DMEM (Invitrogen) supplemented with 1 × 107 U/L penicillin (HyClone), 10 mg/L streptomycin (HyClone), and 10% fetal bovine serum (Invitrogen) in a humidified incubator at 37 °C under 5% CO_2 atm, following cell culture guidelines.

To generate cells that stably expressed TMEM16A (also known as Anoctamin 1), HEK293T cells were infected with lentivirus at 37 °C. After 48 h, the medium was replaced, and puromycin selection (1 mg/mL) was applied to select positive clones for 2 weeks.

4.6. Electrophysiology. We utilized the patch-clamp technique to record TMEM16A currents in whole-cell patches. All patch-clamp experiments were performed at room temperature, 25 °C. Patch pipettes were pulled from borosilicate glass capillaries (BF150-80-10, 1.5 mm × 0.86 mm). The tip of the patch pipet induces a resistance of 2−4 MΩ when filled with the recording solutions. Voltage-clamp recordings were made using a HEKA Epc10 (Germany). The cell capacitance was evaluated by the cell capacitance compensation circuit of the patch-clamp technique when the cell membrane was punctured, and whole-cell recordings formed. Currents were sampled at 20 kHz.

The intracellular solution included 140 mM CsCl, 5 mM EGTA, 2.6 mM $CaCl_2{\cdot}2H_2O$, 10 mM HEPES, and 1 mM $MgCl_2$. CsOH was used to adjust the pH to 7.2. The extracellular solution included140 mM NaCl, 4 mM KCl, 1.8 mM $CaCl_2$, 1 mM MgCl2, 10 mM Glucose, and 10 mM HEPES. NaOH was used to adjust the pH to 7.4. The free Ca^{2+} concentration of the extracellular solution was 300 nM.

https://doi.org/10.1021/jacs.3c11940
J. Am. Chem. Soc. 2024, 146, 4665−4679

Regarding the stimulation protocols, the holding V_m = 0 mV. First, 1.5 s V_m steps depolarized from 0 to 70 mV (prepulse). Then, the current $-V_m$ (I–V) data were constructed by measuring the currents in response to 1 s V_m steps from −100 to +140 mV at an increase of 40 mV (test pulses). For each mutant/wild type, the number of experiments was 5.

■ ASSOCIATED CONTENT

Supporting Information

The Supporting Information is available free of charge at https://pubs.acs.org/doi/10.1021/jacs.3c11940.

Additional details and results; free energy profiles of the CG model; targeted molecular dynamics; plasmid construction and Lentivirus production; western blotting immunostaining and imaging of the confocal microscope; location of important residues in the activation process; residue energy contribution in the process of conformational changes; analysis of E624 and E633; location of important residues in the activation process; explanation of effects of mutation Q649A; explanation of effects of 21 mutations; whole-cell patch-clamp experimental results; comparison of our calculations and experimental results; free energy profiles in the I_1, T_1, I_2, and T_2 states; distance between the center of the channel pore and the pore-lining residues in the neck region of the wild type/mutations; and primer sequences (PDF)

Ion conduction in the whole homodimer (MP4)

Ion conduction in the subunit (MP4)

■ AUTHOR INFORMATION

Corresponding Authors

Song Wu − *South China Hospital, Health Science Center, Shenzhen University, Shenzhen 518116, China;* orcid.org/0000-0003-3504-1630; Email: wusong@szu.edu.cn

Arieh Warshel − *Department of Chemistry, University of Southern California, Los Angeles, California 90089-1062, United States;* orcid.org/0000-0001-7971-5401; Email: warshel@usc.edu

Chen Bai − *Warshel Institute for Computational Biology, School of Life and Health Sciences, School of Medicine, The Chinese University of Hong Kong (Shenzhen), Shenzhen 518172, China; Chenzhu Biotechnology Co., Ltd., Hangzhou 310005, China;* orcid.org/0000-0003-4560-3019; Email: baichen@cuhk.edu.cn

Authors

Yue Zhang − *Warshel Institute for Computational Biology, School of Life and Health Sciences, School of Medicine, The Chinese University of Hong Kong (Shenzhen), Shenzhen 518172, China; School of Chemistry and Materials Science, University of Science and Technology of China, Hefei 230026, China;* orcid.org/0000-0001-9609-7879

Kang Wu − *South China Hospital, Health Science Center, Shenzhen University, Shenzhen 518116, China*

Yuqing Li − *South China Hospital, Health Science Center, Shenzhen University, Shenzhen 518116, China*

Complete contact information is available at: https://pubs.acs.org/10.1021/jacs.3c11940

Notes

The authors declare no competing financial interest.

■ ACKNOWLEDGMENTS

This research was supported by the National Natural Science Foundation of Youth Fund Project (grant number: 22103066); the National Natural Science Foundation of China (grant number: 61931024); and the 2021 Basic Research General Project of Shenzhen, China (grant number: 20210316202830001). A.W. is supported by the National Institutes of Health R35 GM122472 and the National Science Foundation Grant MCB 1707167.

■ REFERENCES

(1) Lin, T.-T.; Zhang, T.; Kitata, R. B.; Liu, T.; Smith, R. D.; Qian, W.-J.; Shi, T. Mass spectrometry-based targeted proteomics for analysis of protein mutations. *Mass Spectrom. Rev.* **2023**, *42* (2), 796−821.

(2) Nisthal, A.; Wang, C. Y.; Ary, M. L.; Mayo, S. L. Protein stability engineering insights revealed by domain-wide comprehensive mutagenesis. *Proc. Natl. Acad. Sci. U.S.A.* **2019**, *116* (33), 16367−16377.

(3) Bugter, J. M.; Fenderico, N.; Maurice, M. M. Mutations and mechanisms of WNT pathway tumour suppressors in cancer. *Nat. Rev. Cancer* **2021**, *21* (1), 5−21.

(4) Bottega, R.; Perrone, M. D.; Vecchiato, K.; Taddio, A.; Sabui, S.; Pecile, V.; Said, H. M.; Faletra, F. Functional analysis of the third identified SLC25A19 mutation causative for the thiamine metabolism dysfunction syndrome 4. *J. Hum. Genet.* **2019**, *64* (11), 1075−1081.

(5) Tsang, B.; Pritišanac, I.; Scherer, S. W.; Moses, A. M.; Forman-Kay, J. D. Phase Separation as a Missing Mechanism for Interpretation of Disease Mutations. *Cell* **2020**, *183* (7), 1742−1756.

(6) Flores, B. N.; Li, X.; Malik, A. M.; Martinez, J.; Beg, A. A.; Barmada, S. J. An Intramolecular Salt Bridge Linking TDP43 RNA Binding, Protein Stability, and TDP43-Dependent Neurodegeneration. *Cell Rep.* **2019**, *27* (4), 1133−1150.e8.

(7) Hassin, O.; Oren, M. Drugging p53 in cancer: one protein, many targets. *Nat. Rev. Drug Discovery* **2023**, *22* (2), 127−144.

(8) Peng, C.; Trojanowski, J. Q.; Lee, V. M. Y. Protein transmission in neurodegenerative disease. *Nat. Rev. Neurol.* **2020**, *16* (4), 199−212.

(9) Liu, J.-J.; Yu, C.-S.; Wu, H.-W.; Chang, Y.-J.; Lin, C.-P.; Lu, C.-H. The structure-based cancer-related single amino acid variation prediction. *Sci. Rep.* **2021**, *11* (1), 13599.

(10) Pandurangan, A. P.; Blundell, T. L. Prediction of impacts of mutations on protein structure and interactions: SDM, a statistical approach, and mCSM, using machine learning. *Protein Sci.* **2020**, *29* (1), 247−257.

(11) Siebenmorgen, T.; Zacharias, M. Computational prediction of protein-protein binding affinities. *Wiley Comput. Mol. Sci.* **2020**, *10* (3), No. e1448.

(12) Warshel, A. Multiscale Modeling of Biological Functions: From Enzymes to Molecular Machines (Nobel Lecture). *Angew. Chem., Int. Ed.* **2014**, *53* (38), 10020−10031.

(13) Reva, B.; Antipin, Y.; Sander, C. Predicting the functional impact of protein mutations: application to cancer genomics. *Nucleic Acids Res.* **2011**, *39* (17), No. e118.

(14) Fang, J. A critical review of five machine learning-based algorithms for predicting protein stability changes upon mutation. *Briefings Bioinf.* **2020**, *21* (4), 1285−1292.

(15) Pucci, F.; Schwersensky, M.; Rooman, M. Artificial intelligence challenges for predicting the impact of mutations on protein stability. *Curr. Opin. Struct. Biol.* **2022**, *72*, 161−168.

(16) McGuinness, K. N.; Pan, W.; Sheridan, R. P.; Murphy, G.; Crespo, A. Role of simple descriptors and applicability domain in predicting change in protein thermostability. *PLoS One* **2018**, *13* (9), No. e0203819.

(17) Liu, J.; Pei, J.; Lai, L. A combined computational and experimental strategy identifies mutations conferring resistance to drugs targeting the BCR-ABL fusion protein. *Commun. Biol.* **2020**, *3* (1), 18.

(18) Fan, X.; Huang, J.; Jin, X.; Yan, N. Cryo-EM structure of human voltage-gated sodium channel Nav1.6. *Proc. Natl. Acad. Sci. U.S.A.* **2023**, *120* (5), No. e2220578120.
(19) Owji, A. P.; Wang, J.; Kittredge, A.; Clark, Z.; Zhang, Y.; Hendrickson, W. A.; Yang, T. Structures and gating mechanisms of human bestrophin anion channels. *Nat. Commun.* **2022**, *13* (1), 3836.
(20) Arrigoni, C.; Lolicato, M.; Shaya, D.; Rohaim, A.; Findeisen, F.; Fong, L.-K.; Colleran, C. M.; Dominik, P.; Kim, S. S.; Schuermann, J. P.; DeGrado, W. F.; Grabe, M.; Kossiakoff, A. A.; Minor, D. L. Quaternary structure independent folding of voltage-gated ion channel pore domain subunits. *Nat. Struct. Mol. Biol.* **2022**, *29* (6), 537−548.
(21) Deng, Y.-n.; Kashtoh, H.; Wang, Q.; Zhen, G.-x.; Li, Q.-y.; Tang, L.-h.; Gao, H.-l.; Zhang, C.-r.; Qin, L.; Su, M.; Li, F.; Huang, X.-h.; Wang, Y.-c.; Xie, Q.; Clarke, O. B.; Hendrickson, W. A.; Chen, Y.-h. Structure and activity of SLAC1 channels for stomatal signaling in leaves. *Proc. Natl. Acad. Sci. U.S.A.* **2021**, *118* (18), No. e2015151118.
(22) Zhou, Z. Structural Analysis of Piezo1 Ion Channel Reveals the Relationship between Amino Acid Sequence Mutations and Human Diseases. *J. Biosci. Med.* **2019**, *07* (12), 139−155.
(23) Jih, K.-Y.; Lin, W.-Y.; Sohma, Y.; Hwang, T.-C. CFTR potentiators: from bench to bedside. *Curr. Opin. Pharmacol.* **2017**, *34*, 98−104.
(24) Ruiz, C.; Martins, J. R.; Rudin, F.; Schneider, S.; Dietsche, T.; Fischer, C. A.; Tornillo, L.; Terracciano, L. M.; Schreiber, R.; Bubendorf, L.; Kunzelmann, K. Enhanced Expression of ANO1 in Head and Neck Squamous Cell Carcinoma Causes Cell Migration and Correlates with Poor Prognosis. *PLoS One* **2012**, *7* (8), No. e43265.
(25) Espinosa, I.; Lee, C.-H.; Kim, M. K.; Rouse, B.-T.; Subramanian, S.; Montgomery, K.; Varma, S.; Corless, C. L.; Heinrich, M. C.; Smith, K. S.; Wang, Z.; Rubin, B.; Nielsen, T. O.; Seitz, R. S.; Ross, D. T.; West, R. B.; Cleary, M. L.; van de Rijn, M. A Novel Monoclonal Antibody Against DOG1 is a Sensitive and Specific Marker for Gastrointestinal Stromal Tumors. *Am. J. Surg. Pathol.* **2008**, *32* (2), 210−218.
(26) Li, S.; Wang, Z.; Geng, R.; Zhang, W.; Wan, H.; Kang, X.; Guo, S. TMEM16A ion channel: A novel target for cancer treatment. *Life Sci.* **2023**, *331*, 122034.
(27) Okuyama, K.; Yanamoto, S. TMEM16A as a potential treatment target for head and neck cancer. *J. Exp. Clin. Cancer Res.* **2022**, *41* (1), 196.
(28) Falzone, M. E.; Malvezzi, M.; Lee, B.-C.; Accardi, A. Known structures and unknown mechanisms of TMEM16 scramblases and channels. *J. Gen. Physiol.* **2018**, *150* (7), 933−947.
(29) Kalienkova, V.; Clerico Mosina, V.; Paulino, C. The groovy TMEM16 family: molecular mechanisms of lipid scrambling and ion conduction. *J. Mol. Biol.* **2021**, *433* (16), 166941.
(30) Caputo, A.; Caci, E.; Ferrera, L.; Pedemonte, N.; Barsanti, C.; Sondo, E.; Pfeffer, U.; Ravazzolo, R.; Zegarra-Moran, O.; Galietta, L. J. V. TMEM16A, A Membrane Protein Associated with Calcium-Dependent Chloride Channel Activity. *Science* **2008**, *322* (5901), 590−594.
(31) Stöhr, H.; Heisig, J. B.; Benz, P. M.; Schöberl, S.; Milenkovic, V. M.; Strauss, O.; Aartsen, W. M.; Wijnholds, J.; Weber, B. H.; Schulz, H. L. TMEM16B, a novel protein with calcium-dependent chloride channel activity, associates with a presynaptic protein complex in photoreceptor terminals. *J. Neurosci.* **2009**, *29* (21), 6809−6818.
(32) Lee, B.-C.; Menon, A. K.; Accardi, A. The nhTMEM16 scramblase is also a nonselective ion channel. *Biophys. J.* **2016**, *111* (9), 1919−1924.
(33) Bushell, S. R.; Pike, A. C. W.; Falzone, M. E.; Rorsman, N. J. G.; Ta, C. M.; Corey, R. A.; Newport, T. D.; Christianson, J. C.; Scofano, L. F.; Shintre, C. A.; Tessitore, A.; Chu, A.; Wang, Q.; Shrestha, L.; Mukhopadhyay, S. M. M.; Love, J. D.; Burgess-Brown, N. A.; Sitsapesan, R.; Stansfeld, P. J.; Huiskonen, J. T.; Tammaro, P.; Accardi, A.; Carpenter, E. P. The structural basis of lipid scrambling and inactivation in the endoplasmic reticulum scramblase TMEM16K. *Nat. Commun.* **2019**, *10* (1), 3956.
(34) Lam, A. K. M.; Rheinberger, J.; Paulino, C.; Dutzler, R. Gating the pore of the calcium-activated chloride channel TMEM16A. *Nat. Commun.* **2021**, *12* (1), 785.
(35) Paulino, C.; Neldner, Y.; Lam, A. K. M.; Kalienkova, V.; Brunner, J. D.; Schenck, S.; Dutzler, R. Structural basis for anion conduction in the calcium-activated chloride channel TMEM16A. *eLife* **2017**, *6*, No. e26232.
(36) Yang, Y. D.; Cho, H.; Koo, J. Y.; Tak, M. H.; Cho, Y.; Shim, W.-S.; Park, S. P.; Lee, J.; Lee, B.; Kim, B.-M.; Raouf, R.; Shin, Y. K.; Oh, U. TMEM16A confers receptor-activated calcium-dependent chloride conductance. *Nature* **2008**, *455* (7217), 1210−1215.
(37) Paulino, C.; Kalienkova, V.; Lam, A. K. M.; Neldner, Y.; Dutzler, R. Activation mechanism of the calcium-activated chloride channel TMEM16A revealed by cryo-EM. *Nature* **2017**, *552* (7685), 421−425.
(38) Dang, S.; Feng, S.; Tien, J.; Peters, C. J.; Bulkley, D.; Lolicato, M.; Zhao, J.; Zuberbühler, K.; Ye, W.; Qi, L.; Chen, T.; Craik, C. S.; Jan, Y. N.; Minor, D. L.; Cheng, Y.; Jan, L. Y. Cryo-EM structures of the TMEM16A calcium-activated chloride channel. *Nature* **2017**, *552* (7685), 426−429.
(39) Jeng, G.; Aggarwal, M.; Yu, W.-P.; Chen, T.-Y. Independent activation of distinct pores in dimeric TMEM16A channels. *J. Gen. Physiol.* **2016**, *148* (5), 393−404.
(40) Lim, N. K.; Lam, A. K. M.; Dutzler, R. Independent activation of ion conduction pores in the double-barreled calcium-activated chloride channel TMEM16A. *J. Gen. Physiol.* **2016**, *148* (5), 375−392.
(41) Lam, A. K. M.; Dutzler, R. Calcium-dependent electrostatic control of anion access to the pore of the calcium-activated chloride channel TMEM16A. *eLife* **2018**, *7*, No. e39122.
(42) Dinsdale, R. L.; Pipatpolkai, T.; Agostinelli, E.; Russell, A. J.; Stansfeld, P. J.; Tammaro, P. An outer-pore gate modulates the pharmacology of the TMEM16A channel. *Proc. Natl. Acad. Sci. U.S.A.* **2021**, *118* (34), No. e2023572118.
(43) Hwang, S. J.; Basma, N.; Sanders, K. M.; Ward, S. M. Effects of new-generation inhibitors of the calcium-activated chloride channel anoctamin 1 on slow waves in the gastrointestinal tract. *Br. J. Pharmacol.* **2016**, *173* (8), 1339−1349.
(44) Kang, J. W.; Lee, Y. H.; Kang, M. J.; Lee, H. J.; Oh, R.; Min, H. J.; Namkung, W.; Choi, J. Y.; Lee, S. N.; Kim, C.-H.; Yoon, J.-H.; Cho, H.-J. Synergistic mucus secretion by histamine and IL-4 through TMEM16A in airway epithelium. *Am. J. Physiol. Lung Cell Mol. Physiol.* **2017**, *313* (3), L466−L476.
(45) Huang, F.; Wong, X.; Jan, L. Y. International Union of Basic and Clinical Pharmacology. LXXXV: Calcium-Activated Chloride Channels. *Pharmacol. Rev.* **2012**, *64* (1), 1−15.
(46) Lee, B.; Cho, H.; Jung, J.; Yang, Y. D.; Yang, D.-J.; Oh, U. Anoctamin 1 Contributes to Inflammatory and Nerve-Injury Induced Hypersensitivity. *Mol. Pain* **2014**, *10*, 1744-8069.
(47) Ji, Q.; Guo, S.; Wang, X.; Pang, C.; Zhan, Y.; Chen, Y.; An, H. Recent advances in TMEM16A: Structure, function, and disease. *J. Cell. Physiol.* **2019**, *234* (6), 7856−7873.
(48) Shi, S.; Pang, C.; Guo, S.; Chen, Y.; Ma, B.; Qu, C.; Ji, Q.; An, H. Recent progress in structural studies on TMEM16A channel. *Comput. Struct. Biotechnol. J.* **2020**, *18*, 714−722.
(49) Lam, A. K. M.; Dutzler, R. Mechanism of pore opening in the calcium-activated chloride channel TMEM16A. *Nat. Commun.* **2021**, *12* (1), 786.
(50) Peters, C. J.; Gilchrist, J. M.; Tien, J.; Bethel, N. P.; Qi, L.; Chen, T.; Wang, L.; Jan, Y. N.; Grabe, M.; Jan, L. Y. The Sixth Transmembrane Segment Is a Major Gating Component of the TMEM16A Calcium-Activated Chloride Channel. *Neuron* **2018**, *97* (5), 1063−1077.e4.
(51) Vicatos, S.; Rychkova, A.; Mukherjee, S.; Warshel, A. An effective Coarse-grained model for biological simulations: Recent refinements and validations. *Proteins: Struct., Funct., Bioinf.* **2014**, *82* (7), 1168−1185.

https://doi.org/10.1021/jacs.3c11940
J. Am. Chem. Soc. 2024, 146, 4665−4679

(52) Vorobyov, I.; Kim, I.; Chu, Z. T.; Warshel, A. Refining the treatment of membrane proteins by coarse-grained models. *Proteins: Struct., Funct., Bioinf.* **2016**, *84* (1), 92−117.
(53) Lee, M.; Kolev, V.; Warshel, A. Validating a Coarse-Grained Voltage Activation Model by Comparing Its Performance to the Results of Monte Carlo Simulations. *J. Phys. Chem. B* **2017**, *121* (50), 11284−11291.
(54) Bai, C.; Wang, J.; Mondal, D.; Du, Y.; Ye, R. D.; Warshel, A. Exploring the Activation Process of the β2AR-G_sComplex. *J. Am. Chem. Soc.* **2021**, *143* (29), 11044−11051.
(55) Bai, C.; Warshel, A. Revisiting the protomotive vectorial motion of F0-ATPase. *Proc. Natl. Acad. Sci. U.S.A.* **2019**, *116* (39), 19484−19489.
(56) Alhadeff, R.; Warshel, A. Reexamining the origin of the directionality of myosin V. *Proc. Natl. Acad. Sci. U.S.A.* **2017**, *114* (39), 10426−10431.
(57) Lee, M.; Bai, C.; Feliks, M.; Alhadeff, R.; Warshel, A. On the control of the proton current in the voltage-gated proton channel Hv1. *Proc. Natl. Acad. Sci. U.S.A.* **2018**, *115* (41), 10321−10326.
(58) Bai, C.; Warshel, A. Critical Differences between the Binding Features of the Spike Proteins of SARS-CoV-2 and SARS-CoV. *J. Phys. Chem. B* **2020**, *124* (28), 5907−5912.
(59) Webb, B.; Sali, A. Comparative Protein Structure Modeling Using MODELLER. *Curr. Protoc. Bioinf.* **2016**, *86* (1), 5.6.1−5.6.37.
(60) Martí-Renom, M. A.; Stuart, A. C.; Fiser, A.; Sánchez, R.; Melo, F.; Šali, A. Comparative Protein Structure Modeling of Genes and Genomes. *Annu. Rev. Biophys. Biomol. Struct.* **2000**, *29* (1), 291−325.
(61) Fiser, A.; Do, R. K. G.; Šali, A. Modeling of loops in protein structures. *Protein Sci.* **2000**, *9* (9), 1753−1773.
(62) Schlitter, J.; Engels, M.; Krüger, P. Targeted molecular dynamics: A new approach for searching pathways of conformational transitions. *J. Mol. Graph.* **1994**, *12* (2), 84−89.
(63) Burykin, A.; Kato, M.; Warshel, A. Exploring the origin of the ion selectivity of the KcsA potassium channel. *Proteins: Struct., Funct., Bioinf.* **2003**, *52* (3), 412−426.
(64) Huang, J.; Chen, J. Hydrophobic gating in bundle-crossing ion channels: a case study of TRPV4. *Commun. Biol.* **2023**, *6* (1), 1094.
(65) Rao, S.; Klesse, G.; Stansfeld, P. J.; Tucker, S. J.; Sansom, M. S. P. A BEST example of channel structure annotation by molecular simulation. *Channels* **2017**, *11* (4), 347−353.
(66) Smart, O. S.; Neduvelil, J. G.; Wang, X.; Wallace, B. A.; Sansom, M. S. P. HOLE: A program for the analysis of the pore dimensions of ion channel structural models. *J. Mol. Graph.* **1996**, *14* (6), 354−360.
(67) Shi, S.; Pang, C.; Ren, S.; Sun, F.; Ma, B.; Guo, S.; Li, J.; Chen, Y.; An, H. Molecular dynamics simulation of TMEM16A channel: Linking structure with gating. *Biochim. Biophys. Acta, Biomembr.* **2022**, *1864* (1), 183777.
(68) De Jesús-Pérez, J. J.; López-Romero, A. E.; Posadas, O.; Segura-Covarrubias, G.; Aréchiga-Figueroa, I.; Gutiérrez-Medina, B.; Pérez-Cornejo, P.; Arreola, J. Gating and anion selectivity are reciprocally regulated in TMEM16A (ANO1). *J. Gen. Physiol.* **2022**, *154* (8), No. e202113027.
(69) Kamerlin, S. C. L.; Vicatos, S.; Dryga, A.; Warshel, A. Coarse-Grained (Multiscale) Simulations in Studies of Biophysical and Chemical Systems. *Annu. Rev. Phys. Chem.* **2011**, *62* (1), 41−64.
(70) Lee, F. S.; Chu, Z. T.; Warshel, A. Microscopic and semimicroscopic calculations of electrostatic energies in proteins by the POLARIS and ENZYMIX programs. *J. Comput. Chem.* **1993**, *14* (2), 161−185.
(71) Warshel, A.; King, G. Polarization constraints in molecular dynamics simulation of aqueous solutions: The surface constraint all atom solvent (SCAAS) model. *Chem. Phys. Lett.* **1985**, *121* (1−2), 124−129.
(72) Lee, F. S.; Warshel, A. A local reaction field method for fast evaluation of long-range electrostatic interactions in molecular simulations. *J. Chem. Phys.* **1992**, *97* (5), 3100−3107.
(73) Muegge, I.; Tao, H.; Warshel, A. A fast estimate of electrostatic group contributions to the free energy of protein-inhibitor binding. *Protein Eng. Des. Sel.* **1997**, *10* (12), 1363−1372.
(74) Schutz, C. N.; Warshel, A. What are the dielectric "constants" of proteins and how to validate electrostatic models? *Proteins: Struct., Funct., Bioinf.* **2001**, *44* (4), 400−417.
(75) Singh, N.; Warshel, A. Absolute binding free energy calculations: On the accuracy of computational scoring of protein-ligand interactions. *Proteins: Struct., Funct., Bioinf.* **2010**, *78* (7), 1705−1723.

https://doi.org/10.1021/jacs.3c11940
J. Am. Chem. Soc. 2024, 146, 4665−4679